

APPLICATION OF THE THEORY OF CRITICAL DISTANCES FOR THE FRACTURE ASSESSMENT OF A NOTCHED LIMESTONE SUBJECTED TO DIFFERENT TEMPERATURES AND MIXED MODE WITH PREDOMINANT MODE I LOADING CONDITIONS.

J. Justo^{a*}, J. Castro^a, S. Cicero^b

^aGroup of Geotechnical Engineering, Universidad de Cantabria, E.T.S de Ingenieros de Caminos, Canales y Puertos, Av/ Los Castros 44, 39005, Santander, Spain

^bLADICIM (Laboratory of Materials Science and Engineering), Universidad de Cantabria, E.T.S de Ingenieros de Caminos, Canales y Puertos, Av/ Los Castros 44, 39005, Santander, Spain

* Contact person: justoj@unican.es

ABSTRACT

This work aims to assess the fracture of U-notched limestone samples subjected to mixed mode I+II loading conditions with a predominant mode I influence, both at room temperature and at 250°C. This analysis is based on the use of the Theory of the Critical Distances, and more specifically on the use of the Line Method, considering both an analytical and a numerical approach for the definition of the stress fields. An experimental campaign of almost 400 three-point bending tests has been performed as a basis for the fracture assessment of the limestone, using Single Edge Notched Bend (SENB) specimens with notch radii varying from 0.15 mm up to 15 mm, different temperature conditions and variable loading positions. The Theory of Critical Distances has successfully been applied to study the experimental results. The analytical and numerical stress fields for pure mode I fracture assessments provide similar accurate results both at 23°C and 250°C. Similarly, the mixed mode (I+II) fracture assessments allow the critical distance (L) to be characterised for different mode mixities (M_e), using the stress field around the notch tip obtained from the numerical models. Comparing the values of the critical distance against the mode mixity in isolation, a slight decrease of L is observed as it approaches pure mode I conditions ($M_e = 1$). However, if the results are analysed separately for each notch radius, L seems to be relatively constant with M_e . In parallel, a certain influence of the notch radius on the critical distance is appreciated, which shows an increment both at 23°C and 250°C.

Keywords: rock; limestone; notch; brittle fracture; Theory of Critical Distances; mixed mode loading

Abbreviations

BD	Brazilian Disc
CZM	Cohesive Zone Model
ECT	Edge Cracked Triangular
ENDB	Edge-Notched Disc Bend
LEFM	Linear Elastic Fracture Mechanics
LM	Line Method
MTS	Maximum Tangential Stress
MTSN	Maximum Tangential Strain
NSIF	Notch Stress Intensity Factor
SCB	Semi-Circular Bend
SED	Strain Energy Density
SENB	Single Edge Notched Bend
TCD	Theory of Critical Distances

List of symbols

A, B	Material dependent constant parameters
a_0	Initial notch length
b	Thickness of the specimen
d	Distance over which the stress is averaged in the LM ($d = 2L$)
E_{50}	Tangent Young's modulus at 50% of the peak load
F	Load
F_{EXP}	Experimentally obtained failure load
F_{TCD}	Fracture load prediction according to the TCD
h	Specimen height
K_I	Stress Intensity Factor
K_I^u, K_{II}^u	Mode I and mode II generalised NSIFs
K_{IC}	Fracture toughness (mode I)
K_{IN}	Apparent fracture toughness (mode I)
L	Critical distance
m	Distance between the applied load position and the notch bisector plane
M_e	Mode mixity
r, θ	Polar coordinate system
r_0	Distance between notch tip and the origin of the polar coordinate system
x	Distance from the notch tip
Y	Non-dimensional factor

Greek Letters

ν	Poisson's ratio
ρ	Notch radius
σ_0	Inherent strength of the material
$\sigma_r, \sigma_\theta, \tau_{r\theta}$	Stress state according to the polar coordinate system
σ_u	Ultimate tensile strength of the material

1. INTRODUCTION

One of the main aspects characterising a rock from a mechanical point of view is the predominantly brittle fracture behaviour. Quasi-brittle materials like rocks display very limited non-linear behaviour before failure and, therefore, crack propagation is unstable and leads to sudden fast fracture. This condition can lead to catastrophic failure in cracked rock masses and structures. For this reason, efficient criteria to perform accurate rock fracture assessments is a major issue of interest in many practical rock engineering applications such as, for example, rock excavations, tunnelling, rock cutting processes, hydraulic fracturing, rock slope or well stability analyses, etc., especially when stress concentration phenomena are involved.

Crack-type defects, those with a theoretical tip radius equal to zero, develop more demanding stress fields than notch-type defects (i.e., those with a finite radius on the tip). As demonstrated by different authors (e.g., Taylor 2007; Justo et al. 2017), when the notch radius is sufficiently small the notch effect is almost negligible. However, according to Taylor (2007), when the notch radius is of the order of the critical distance of the material, the notch effect becomes more evident. In the particular case of rocks, this condition is generally fulfilled with a few millimetres (Justo et al. 2017). Thus, neglecting the notch effect and proceeding on the assumption that all the defects behave as crack-type defects may be overly conservative in many real cases. Different underground engineering problems such as tunnels, mines, wells,

etc. can be generally studied as sharp V-shaped notches, U-shaped notches or as intermediate situations like rounded V-shaped notches. For this reason, the influence of the notch geometry on the fracture behaviour of different components has been widely studied (e.g., Gómez and Elices 2003; Gómez et al. 2006).

The singular stress fields generated by the presence of cracks and notches cannot be directly assessed by simply determining the linear-elastic maximum principal stress at the crack initiation site (Susmel and Taylor 2008). Hence, in recent years, many researchers have attempted to predict static strength in cracked and notched brittle components based on the use of linear elastic fracture mechanics (LEFM) theory. Dealing with the fracture of notched elements, different stress, strain and energy based theories and criteria can be found in the literature. Among others, the generalised stress intensity factors have been extensively used for the fracture assessment of brittle notched elements (e.g., Carpinteri 1987; Seweryn 1994; Nui et al. 1994; Dunn et al. 1997). Gomez et al. (2000) proposed a cracking criterion for the assessment of critical static loads for U-notched components, extending the Cohesive Zone Model (CZM) proposed in the past by Dugdale (1960) and Barenblatt (1962). In parallel developments, Lazzarin and Zambardi (2001) used the average Strain Energy Density (SED) concept to predict the static and fatigue behaviour of sharp V-notched components, which is based on the elementary volume proposed by Neuber (1958) and the local mode I concept first proposed by Erdogan and Sih (1963). On the other hand, the use of stress values within a material-dependent critical length from the notch tip is also extended in the area of brittle fracture (Neuber 1958; Tanaka 1983; Sheppard 1991; Radaj 2013). In this last group, the Theory of Critical Distances (TCD) has proved to be a useful engineering tool for predicting the failure of notched elements (Vargiu et al. 2017). It was originally developed, in terms of stresses, by Neuber (1958) and Peterson (1959) for the fatigue assessment of metallic materials. Later, the TCD was successfully extended by Taylor (Taylor 2004; Taylor et al. 2004; Taylor 2006) to the static assessment of notched brittle materials subjected to mode I loading. Initially, all these methods were systematically used under Mode I loading. However, the highly accurate results obtained by their practical applications suggested that such methods could also be used under mixed-mode loading conditions (Dunn et al. 1997b; Seweryn et al. 1997; Gómez et al. 2007; Berto et al. 2007).

In the particular field of rock fracture mechanics, the scientific contributions dealing with the applications of the aforementioned criteria for the fracture assessment of notched rocks are less abundant and fairly recent (e.g., Justo et al. 2017; Justo et al. 2019; Aliha et al. 2019; Nejati et al. 2020), probably due to the relatively large scatter of the experimental results as a consequence of the higher degree of heterogeneity of rocks compared to metallic or polymeric materials, for example. It is generally accepted that crack propagation phenomena in rocks are mode I dominated. This is caused by the relatively small tensile resistance of rocks that makes them highly sensitive to opening loading (mode I). However, rock masses are usually subjected to complex loading conditions and the defects within the rock are randomly orientated. For this reason, in many practical situations the influence of combined opening-sliding shear deformations (i.e., mixed mode I+II) needs to be studied. Aliha et al. (2017), for example, were some of the first researchers studying the applicability of the average SED criterion on rock materials subjected to mixed I+II loading conditions. Similarly, Mirsayar et al. (2018) evaluated mixed mode I+II crack propagation in rock materials using an extended version of the maximum tangential strain (MTSN) criterion, and Sangsefidi et al. (2020) presented an approach based on the maximum tangential stress (MTS) criterion to predict the mixed-mode fracture resistance of U-notched rock-type specimens. However, to the best knowledge of the

authors, the TCD has not been applied yet in the field of rock fracture mechanics under mixed mode loading conditions.

One of the greatest advantages of the TCD consists of the possibility of obtaining (semi-) analytical results to correctly perform static assessment without loss of accuracy (Cornetti et al. 2016). The authors have successfully applied the TCD (Justo et al. 2017) for the fracture assessment of several notched rocks under mode I loading, based on the results of Single Edge Notched Bend (SENB) specimens subjected to four-point bending conditions. Besides, the authors (Justo et al. 2020) have also applied the TCD for the fracture assessment of several rocks up to approximately 250°C, which is, for example, an expected range for conventional high-level radioactive waste disposal (e.g., Ramsrott et al. 1979) and for conventional or hot fracture rock geothermal energy systems (e.g., Ranjith et al. 2012). This work aims to extend those previous authors' researches to analyse the same type of rock specimens subjected to mixed mode (I+II) loading conditions with a predominant mode I influence. To do so, SENB specimens subjected to three-point bending conditions are used here.

A wide variety of test specimens can be found in the literature to investigate different ranges of mode mixities from pure mode I to pure mode II loading conditions. Traditionally, disc and cylindrical shape specimens have been used in the case of geomaterials like rocks, because they can be easily extracted from cylindrical cores. This is the case, for example, of Brazilian disc BD (e.g., Ayatollahi and Aliha 2008), semi-circular bend SCB (e.g., Aliha and Ayatollahi 2013) or edge-notched disc bend ENDB (e.g., Bahmani et al. 2020) specimens. However, with the development of technology that facilitates the preparation of other specimen geometries, different test configurations are also widely and suitably used nowadays, such as edge cracked triangular ECT specimens (e.g., Aliha et al. 2013) or SENB specimens subjected to four-point bending (e.g., Aliha et al. 2009) or three-point bending (e.g., Xeidakis et al. 1996) conditions. In the particular case of SENB specimens, as those used in this work, different mode mixities can be achieved by means of non-centred loads and/or by inclined cracks or notches (e.g., Negru et al. 2015; Mousavi et al. 2020). In particular, SENB specimens with centered straight U-notches are considered here, subjected to three-point bending loading with variable loading position. This configuration allows to obtain pure mode I and mixed mode I+II (with dominant mode I) conditions, and has been chosen to keep the same specimen geometries and same notch sizes as those studied by the authors in previous works under pure mode I four-point bending conditions (e.g., Justo et al. 2017; 2020), for comparison purposes. Rectangular beam specimens with inclined notches would allow to reach up to pure mode II loading conditions (e.g., Aliha and Mousavi 2020), but this is left for future research.

The research focuses on the fracture results of a Moleanos limestone, whose fracture behaviour under four-point bending (pure mode I) loading conditions have already been studied by the authors (Justo et al. 2017; 2020). The limestone rock material has been used in previous research works for investigating mode I and mixed mode fracture behaviour. Aliha et al. (2010; 2012) and Akbardoost et al. (2014), for example, studied the fracture behaviour of Guiting limestone under mixed mode I+II, using both BD and SCB specimens with different sizes. They obtained mode I fracture toughness values (K_{IC}) at room temperature oscillating from 0.18 to 0.53 MPa·m^{1/2}, depending on the specimen type and size. By contrast, Cicero et al. (2014) studied an oolitic limestone using SENB specimens subjected to four-point bending conditions and obtained a K_{IC} value of 0.72 MPa·m^{1/2}. A similar value (i.e., $K_{IC} = 0.73$ MPa·m^{1/2}) was obtained for the Moleanos limestone using the same type of specimens and

test configuration (Justo et al. 2017), in both cases at room temperature. This last value of K_{IC} for the Moleanos limestone increased to $1.07 \text{ MPa}\cdot\text{m}^{1/2}$ when performing those same tests at 250°C , as indicated by Justo et al. (2020). The increment of the fracture toughness with temperature is attributed to the microstructure of the limestone, which is a porous rock. For moderate temperature increments, the closure of pores and preexisting microcracks due to the thermal expansion of grains lead to an increase of the fracture toughness. This phenomenon is obviously limited and once a certain critical temperature is reached, the progressive thermal increase generates new microcracks (as a consequence of the differential thermal expansion of adjacent grains with no space for growth) and the subsequent reduction of the fracture toughness (e.g., Al-Shayea 2000).

In short, this paper assesses the fracture behaviour of a Moleanos limestone subjected to mixed mode (I+II) loading conditions (with mode I predominance) both at room temperature and at 250°C . To do so, the research is based on an exhaustive laboratory campaign comprising numerous tensile splitting tests and three-point bending tests with different loading positions and notch radii (from 0.15 mm up to 15 mm). These test configurations allow to analyse not only the fracture behaviour of the rock under different multiaxial static loading conditions but also the notch effect. For the interpretation of the results, the so called TCD is used together with conventional linear-elastic finite element analyses. The results obtained from the present laboratory campaign are then compared with those obtained in previous works (Justo et al. 2020) for the same type of specimens subjected to four-point bending conditions.

Subsequently, Section 2 provides a brief description of the performed experimental program, defining the analysed rock and the executed laboratory tests. Section 3 focuses on the theoretical basis of the TCD, explaining the analytical and numerical approaches followed in this work for the fracture assessment of notched rocks under pure mode I and mixed mode (I+II) loading conditions. Section 4 collects the obtained results and the corresponding discussion and, finally, Section 5 provides the main conclusions of the research.

2. EXPERIMENTAL PROGRAM

The experimental program was performed on a Moleanos limestone, which is classified as an intrasparitic-pelsparitic limestone (Folk 1959) from a petrographic point of view. This rock is a compound of subrounded-rounded intraclasts, bioclasts formed by fragments of bivalves and corals, pellets as the dominant allochemical component and sparite crystals that totally cement the allochemical components. Fig. 1, which was obtained with an optical microscope using thin sections of the Moleanos limestone, shows its microstructure.

The mechanical and fracture behaviour of this rock was previously studied by the authors (Justo et al. 2017; 2020). Accurate load fracture predictions under mode I loading conditions were obtained at different temperatures (up to 250°C), where a linear-elastic behaviour was observed at the whole studied range of temperatures (Justo et al. 2020).

2.1. Tensile splitting tests

A successful application of the TCD requires a proper characterisation of the tensile strength of the studied rock. The tensile strength of the Moleanos limestone was experimentally obtained by the authors both at room temperature and at 250°C in previous

works (Justo et al. 2017; 2020). Besides, some additional tests have been performed in this work to confirm there were no significant differences between the rock blocks of this experimental campaign and the previous ones. In total, 30 tensile splitting (Brazilian) tests have been used to define this parameter, executed according to the ASTM D3967 standards (2016).

64 mm diameter disc specimens with a depth/diameter ratio of 0.5 have been tested, using standardised curved platens to apply the load (Fig. 2a). Besides, the tests were carried out both at room temperature (24 tests) and at 250°C (6 tests), following the same procedure in both cases. Those tests corresponding to 250°C were performed inside a heat chamber to guarantee constant temperature conditions throughout the tests. Moreover, the specimens were preheated to the target temperature at least 48 hours before testing to ensure homogeneous temperature within the rock samples. Fig. 3a shows the experimental setup of the performed Brazilian tests.

2.2. Three-point bending tests of notched specimens

The fracture assessment of the Moleanos limestone under mixed modes I+II was carried out on Single Edge Notched Bend (SENB) specimens subjected to three-point bending conditions. The specimens are 180x30x30 mm size parallelepiped beams with straight U-shaped notches in the middle, as those depicted in Fig. 2b and Fig. 4. 384 tests have been performed in total using different notch radii ($\rho = 0.15$ mm, 0.5 mm, 1 mm, 2 mm, 4 mm, 7 mm, 10 mm and 15 mm) and loading positions.

The ratio between the initial notch length ($a_0 = 15$ mm approximately) and the total height ($h = 30$ mm) of the specimen guarantees high in-plane constraint conditions in all the cases ($0.45 \leq a_0/h \leq 0.55$) despite the small variations in the a_0 values caused by the precision of the cutting process. The smallest notches, those with ρ equal to 0.15 and 0.5 mm, were manufactured using rotating diamond wires, while the rest of the notches were made using abrasive discs with semi-circular contour.

The distance between the symmetry axis and the applied load (F) was varied to represent different degrees of mode mixities, namely $m = 0$ (centred), 4, 8 and 12 mm. Those tests with the centred load ($m = 0$) allow pure mode I conditions to be obtained, and those with the displaced load configurations generate different mixed mode I+II loading conditions with a predominant mode I loading influence. All these tests have been repeated for each notch radius, both at room temperature (approx. 23°C) and at 250°C. Besides, in order to contemplate the variability of the tests due to the heterogeneous nature of the rock, a repetitiveness of 6 tests has been considered for each temperature, load position and notch radius combination. Fig. 3b shows the experimental setup of the performed three-point bending tests. Once again, those tests performed at 250°C were carried out inside a heat chamber after preheating the specimens during 48 hours. The chamber was coupled to a hydraulic press (Fig. 3c), which applies the load under displacement control. All these tests were conducted under a loading rate of 0.05 mm/min till failure according to the European Standards EN 12372 (2006), recording the load-displacement curves. Table 1 gathers a summary of the considered variables in the three-point bending tests. Likewise, the individual test results are collected in Appendix A, where the nomenclature of each test corresponds to the combination of the variables shown in Table 1.

3. ANALYTICAL BASIS

The TCD represents a group of methods with some common features, such as the use of linear elastic analyses when performing fracture assessments and the use of a material-dependent parameter called the critical distance (L) (Taylor 2007). Basically, all the methods within the TCD postulate that failure occurs when a distance dependent equivalent stress reaches the inherent strength (σ_0) of the material. This equivalent stress is equal to the maximum principal stress calculated either at a certain distance from the notch tip (point method), averaged over a distance (line method), over an area (area method) or over a finite volume (volume method), all those criteria being related to the critical distance L . The expression for the critical distance is as follows (Taylor 2007):

$$L = \frac{1}{\pi} \left(\frac{K_{IC}}{\sigma_0} \right)^2 \quad (1)$$

K_{IC} being the material fracture toughness.

Here, the line method (LM) will be used due to the good results provided in previous fracture analyses performed by the authors in several rocks (Justo et al. 2017; Justo et al. 2020). This local failure criterion states that the average stress over a distance (d) is limited by σ_0 which, in the case of quasi-brittle materials like rocks (i.e., a quasi linear-elastic behaviour up to fracture), is roughly equal to the ultimate tensile strength (σ_u) of the material. Besides, it can be analytically demonstrated that the distance d over which the stress is averaged is equal to two times the critical distance ($d = 2L$) (Taylor 2007). Thus, the failure criterion established by the LM can be written as follows:

$$\frac{1}{2L} \int_0^{2L} \sigma(x) dx = \sigma_u \quad (2)$$

where x is the distance from the notch tip as represented in Fig. 5.

3.1. Mode I

The application of the LM for those notched samples subjected to pure mode I loading conditions, that is, with the centred load ($m = 0$), is relatively easy, since the stresses are directly analysed along the bisector of the notch. The stress field can be obtained either analytically, using existing analytical expression for mode I loading conditions, or numerically. In this work both possibilities are studied and compared.

3.1.1. Analytical approach

First, the stress field may be analytically obtained using the stress intensity factor (SIF) and the stress distribution proposed by Creager and Paris (1967) as a function of distance from the notch tip (x) and the notch radius (ρ):

$$\sigma(x) = \frac{K_I}{\sqrt{\pi}} \frac{2(x + \rho)}{(2x + \rho)^{3/2}} \quad (3)$$

Under notched conditions, fracture occurs when the SIF is equal to the apparent fracture toughness ($K_I = K_{IN}$). Thus, the problem is equated to a cracked situation in which K_{IN} is considered instead of the real fracture toughness (K_{IC}). From a strict point of view, K_{IC} corresponds to a cracked situation in which the notch radius is equal to zero ($\rho = 0$). However,

when the notch radius is sufficiently small not to develop a notch effect (Justo et al. 2017), it can be assumed that $K_{IN} = K_{IC}$.

Anderson (2005) developed the following formulation for the calculation of the apparent fracture toughness values (K_{IN}) of the SENB specimens depicted in Fig. 2b and subjected to three-point bending tests with a centred load ($m = 0$):

$$K_{IN} = \frac{F}{b\sqrt{h}}Y \quad (4)$$

where F is the failure load of the three-point bending tests, b (30 mm) and h (30 mm) are the specimen depth and height, respectively, and Y is a non-dimensional factor given by the following expression (Anderson 2005):

$$Y = \frac{15\sqrt{\frac{a_0}{h}}}{2\left(1 + 2\frac{a_0}{h}\right)\left(1 - \frac{a_0}{h}\right)^{3/2}} \left\{ 1.99 - \frac{a_0}{h} \left(1 - \frac{a_0}{h}\right) \left[2.15 - 3.93\left(\frac{a_0}{h}\right) + 2.7\left(\frac{a_0}{h}\right)^2 \right] \right\} \quad (5)$$

Considering the LM criterion, the following expression relates the apparent fracture toughness with the critical distance of the material (Taylor 2007):

$$K_{IN} = K_{IC} \sqrt{\frac{\rho}{4L} + 1} \quad (6)$$

K_{IC} is experimentally obtained from those samples with the smallest notch radius ($\rho = 0.15$ mm), assuming a negligible notch effect. Eq. (6) is theoretically only valid for long and narrow notches, as it is based on Eq. (3) of Creager and Paris (1967). However, this expression provided accurate results even beyond the application range of Eq. (3) in several rock fracture assessments performed by the authors (Justo et al. 2017; Justo et al. 2020).

With all this, once the value of the critical distance (L) is defined either by using Eq. (1) or from the best adjustment of the experimentally obtained K_{IN} values according to Eq. (6), any fracture prediction (F_{TCD}) can be performed by simply reversing Eq. (4) (Justo et al. 2020):

$$F_{TCD} = \frac{b\sqrt{h}}{Y} K_{IC} \sqrt{\frac{\rho}{4L} + 1} \quad (7)$$

All these analytical expressions are only valid under pure mode I conditions and cannot be applied to mixed modes. For this reason, a second alternative is studied in this work based on numerical analyses.

3.1.2. Numerical approach

On the basis of Eq. (2), the value of the critical distance (L) can be derived from the tensile strength of the rock (σ_u), which is experimentally obtained in this work, and from the stress field in the surroundings of the notch tip. The required stress distributions are obtained here from linear-elastic finite element analyses performed with PLAXIS 2D 2017 (Brinkgreve et al. 2017), for which plane strain conditions are considered. One model has been constructed for each notch radius and loading position, using triangular 15-node finite elements for the meshing criterion, with a refined region around the notch tip as shown in Fig. 6. All the boundaries of the models were set as free contours, except for the two supporting points that were fixed (one of them in the vertical and horizontal directions and the other one only in the vertical direction). These points are located at the same position as the rollers of the actual

tests, as shown in Fig. 2b. Finally, the load is applied as a point linear load at the positions indicated above.

The linear-elastic models are defined by only two parameters: the Young's modulus (E_{50}) and the Poisson's ratio (ν). The used parameters were experimentally obtained by the authors in a previous work (Justo et al. 2021) from uniaxial compression tests on the same Moleanos limestone, both at room temperature and at 250°C. These parameters are collected in Table 2.

The values of the Young's moduli do not affect the obtained stress fields, but the Poisson's ratio does have an influence on them. Due to the linear elastic behaviour, the response is proportional to the load, and for simplicity, a unity load of 1 N/m has been introduced in all the models according to the different load positions represented in Fig. 2b. Consequently, the required stresses at the bisector of the notches are rescaled according to the obtained failure loads. By simply applying Eq. (2) to the resultant stress fields at the bisector plane, the value of the critical distance (L) can be derived for each numerical model.

3.2. Mixed mode I+II

The application of the LM of the TCD is somehow more complicated for the tested mixed mode loading conditions because of the general lack of analytical solutions for mixed mode problems. However, these problems can be studied numerically as in the case of mode I loading but with certain differences.

3.2.1. Mode Mixity

The opening-sliding shear mixed mode (I+II) fracture investigation on notched specimens requires the characterisation of the mode mixity (M_e). $M_e = 1$ stands for pure mode I loading conditions while $M_e = 0$ corresponds to pure mode II. This dimensionless parameter was introduced by Ayatollahi and Torabi (2009) as an extension of the concept used for cracked geometries and, for the particular case of U-shaped notches, can be calculated with the following expression:

$$M_e = \frac{2}{\pi} \tan^{-1} \left(\frac{K_I^u}{K_{II}^u} \right) \quad (8)$$

where K_I^u and K_{II}^u are, respectively, the mode I and mode II generalised Notch Stress Intensity Factors (NSIF). These parameters are evaluated along the notch bisector according to Lazzarin and Filippi (2006) proposed formulas:

$$K_I^u = \sqrt{2\pi r} \frac{(\sigma_\theta)_{\theta=0}}{1 + r_0/r} \quad (9)$$

$$K_{II}^u = \sqrt{2\pi r} \frac{(\tau_{r\theta})_{\theta=0}}{1 + r_0/r} \quad (10)$$

r and θ are the polar coordinates for the system depicted in Fig. 7, and σ_θ and $\tau_{r\theta}$ are the stresses at the distance r from the local origin defined by r_0 , which varies with the notch radius (ρ). The stress distributions (σ_θ and $\tau_{r\theta}$) along the bisector of the notch were obtained performing linear elastic finite element analyses under plane strain conditions, using the software PLAXIS 2D 2017 (Brinkgreve et al. 2017) as shown in Fig. 6.

Both Eqs. (9) and (10) are an extension of Gross and Mendelson's (1972) definition for sharp V-notches to U-notches. However, the original definitions for the NSIFs given by Gross

and Mendelson (1972) are based on Williams's (1952) solution which matches exactly the stress distributions for ideally sharp V-shaped notches, while Eqs. (9) and (10) are approximate because they are based on the analytical approach proposed by Filippi et al. (2002) to describe the local stress field ahead of rounded V-notches (U-notches being a particular case of rounded V-notches with an opening angle of zero degrees). This approach satisfies the boundary conditions not on the entire free edge but at the notch tip and at a convenient distance from it (Filippi et al. 2002).

Thus, Eqs. (9) and (10) are not expected to give a constant value for the NSIFs, but they will rather show an oscillating value ahead of the notch tip. The entity of this oscillation was analysed by Lazzarin and Filippi (2006), who recommended computing the mean values of K_I^u and K_{II}^u over a distance of 0.4 times the notch radius from the notch tip along the bisector, in order to eliminate the weak dependence on the notch tip distance. This proposal has been validated by Lazzarin and Filippi (2006) and Negru et al. (2015) for notch radii up to 2.5 mm, providing accurate solutions. However, for the notch radii considered in the present work (up to 15 mm), the previous approach does not provide representative K^u values, given that at a distance of 0.4 times the notch radius, the NSIF field is far from being acceptably constant, as shown in Fig. 8. This figure represents the variation of the NSIFs (both K_I^u and K_{II}^u) versus the distance from the notch tip for different notch radii ($\rho = 1, 4$ and 15 mm) and loading configurations ($m = 0$ and 12 mm).

For this reason, in this work the following expression is proposed to determine the distance (x) at which the NSIF must be evaluated:

$$x = 0.4\rho \left(1 - \frac{0.4\rho}{0.4\rho + 0.8mm} \right) \quad (11)$$

This equation provides values very close to 0.4 times the notch radius for notch radii below 2.5 mm, in agreement with Lazzarin and Filippi (2006) and Negru et al. (2015), and generates assessment limits located within the nearly constant NSIF field for larger radii, such as those considered in this work and represented in Fig. 9 by dashed vertical lines.

So, in short, both Eqs. (9) and (10) are evaluated from the notch tip to a distance defined by Eq. (11) and the mode mixity M_e is subsequently calculated with Eq. (8). It can be concluded from Fig. 8 that M_e depends on the loading position and on the notch radius for those cases in which the load is not centred.

Table 3 gathers the calculated values of the mode mixity (M_e) for each of the numerical models according to Eq. (8). It is observed that M_e reduces or, in other words, the mode II influence gets more evident as the loading position moves away from the centre and as the notch radius is larger. The small discrepancies that contradict these trends are caused by the sensitivity of the smallest notches when calculating the NSIFs (Eqs. 9 and 10), as the number of calculation points along the assessed distance from the notch tip (Eq. (11)) is relatively small in the case of the smallest notches (Fig. 8).

3.2.2. Application of TCD

The application of the LM under mixed mode follows a similar approach as the numerical one presented above for mode I. Finite element analyses were performed under the same conditions, with the only difference that the bisector of the notch is no longer the critical plane for mixed mode (I+II) loading conditions, as indicated in Fig. 9.

The main problem to be addressed is the definition of the plane where the stress field must be evaluated under mixed mode, for which the origin (hot spot) and the orientation of the focus path must be specified. It is generally accepted that the static fracture processes take place in highly stressed regions, as those generated by the notches. Accordingly, the superficial point experiencing the largest stress is usually taken as the starting point of the critical plane, which continues perpendicular to the maximum principal stress (Louks et al. 2016). Thus, the hot spot is characterised as the point on the circumference of the U-notch with the highest maximum principal stress (corresponding to the notch tip for mode I loading conditions). Starting from this point, the stress versus distance curve in which Eq. (2) of the LM is assessed is plotted along the plane normal to the maximum principal stress. This plane goes along the centre of the semicircular U-notch. Fig. 10 shows, as an example, the critical planes obtained from the numerical models for two particular cases with $\rho = 1$ mm and different loading positions ($m = 0$ and $m = 12$ mm).

Negru et al. (2015), based on in the degree of multiaxiality concept introduced by Susmel and Taylor (2008), proposed the following equation that links the critical distance with the mode mixity (M_e) to study mixed modes I+II:

$$L = A \cdot M_e + B \quad (14)$$

where A and B are material dependent constant parameters.

4. RESULTS AND DISCUSSION

4.1. Experimental results

The tensile strength results (σ_u) obtained from the Brazilian tests for the Moleanos limestone are collected in Table 4, indicating the mean value and the standard deviation both for those tests performed at room temperature and at 250°C.

Likewise, Table 5 gathers the experimentally obtained average failure loads (F_{EXP}) of the three-point bending tests for each temperature, notch radius and loading position.

In order to verify that no significant inelastic deformations are produced and that the use of LEFM is still valid even at 250°C, some representative load-displacement curves of the three-point bending tests have been analysed in Fig. 11. Each column corresponds to a particular notch radius ($\rho = 0.15, 2, 7$ and 15 mm), while each row corresponds to the two extreme loading positions, namely $m = 0$ and 12 mm. The solid and dashed curves stand for the room temperature and the 250°C results, respectively. The initial non-linear part of the curves that is observed in some cases up to approximately a load of 20 N is associated to the test procedure itself, caused by the initial adjustment of the testing device on the specimen. Consequently, this region should be ignored in terms of deformation but not in terms of load. In general, the tested Moleanos limestone shows a linear elastic behaviour up to the peaks, revealing mostly brittle characteristics even at 250°C.

It can be concluded from the results collected in Table 5 and the curves depicted in Fig. 11 that, in general terms, the load-bearing capacity of the Moleanos limestone increases with temperature and with the notch radius, as expected from previous experiences in four-point bending tests (Justo et al. 2020). Likewise, the load-bearing capacity also increases as the loading position moves away from the centre, as expected. That is, under pure mode I loading conditions the resistance seems to be lower than in those configurations with mode II loading

influence, because the mode I component, to which the onset of rock fracture is especially sensitive, is reduced.

From those three-point bending tests with the smallest notch radius ($\rho = 0.15$ mm), assuming that the radius is sufficiently small not to develop a notch effect, the fracture toughness (K_{IC}) of the Moleanos limestone is calculated using Eq. (4). This hypothesis was already validated by the authors (Justo et al. 2017). Table 6 collects the obtained mean fracture toughness and standard deviations for both room temperature and 250°C. These values are compared with those obtained in the four-point bending tests (Justo et al. 2020). The fracture toughness increases from 23°C to 250°C and consistent results are obtained with both types of tests.

Eventually, Fig. 12 provides some representative Moleanos limestone fractured specimens from the performed three-point bending test, both at room temperature and at 250°C. As mode I is predominant in the studied loading configurations, the fracture planes are relatively vertical. However, it can be observed that fracture trajectories are somehow affected by the loading position and the fracture starting point roughly coincides with the theoretical hot spots. As expected, the fracture planes tend to incline as the loading position moves away from the notch bisector plane (to the left in Fig. 12), or in other words, when mode II influence increases. Finally, temperature does not seem to have any strong influence on the fracture trajectories.

4.2. Interpretation of mode I results

Dealing first with the interpretation of the mode I results, two different procedures have been followed as mentioned above, based on an analytical and a numerical approach. The analytical approach analyses the variation of the apparent fracture toughness (K_{IN}) with the notch radius (ρ) of the tested specimens under three-point bending conditions, only for those cases with $m = 0$ mm (centred load). Accordingly, Fig. 13 represents K_{IN} versus the square root of the notch radius (simply for a better visualisation), both for room temperature and for 250°C. The dots correspond to each of the individual test results calculated with Eq. (4). The dashed lines correspond to the calculated curves according to the LM of the TCD represented by Eq. (6), where L is calculated using Eq. (1) and the parameters collected in Tables 2 and 6. By contrast, the solid lines correspond to the best-fit (least squares) curves based, once again, on Eq. (6), in which the value of the critical distance (L) is left as the free variable. In general terms, a good agreement is observed between the calculated and the best-fit curves in both cases. The detected differences can be caused by the fact that the largest notches studied are beyond the application range of the stress distribution of Creager and Paris (1967), in which Eq. (4) is based. However, relatively good results are obtained even for the largest notches and, from a practical point of view, the consequences of these variations are rather limited, since the critical distance is square rooted in Eq. (6) and, consequently, also in Eq. (7) when performing fracture predictions. In the case of the results corresponding to 23°C, if the best-fit curve was adjusted using only the long and narrow notches (e.g., up to $\rho = 4$ mm) strictly fulfilling the Creager and Paris (1967) stress distribution conditions, both the calculated curve and the best-fit curve would show a better match.

The notch effect can clearly be seen in these graphs, as the apparent fracture toughness increases with the notch radius. Besides, the curves rise from 23°C to 250°C, which means that the fracture toughness increases with temperature as observed in Table 6. The increase of the fracture toughness with temperature is consistent with the increase of the load-bearing

capacity shown in Table 5. This increment of the limestone resistance is caused by the closure of pores and preexisting microcracks as a consequence of the thermal expansion of the grains. This micromechanism has already been reported in previous works investigating the fracture behaviour of porous rocks with temperature, as for example in the case of the Khuff limestone studied by Al-Shayea et al. (2000). Going back to the results depicted in Fig. 13, the curves are approximately parallel at both temperatures, which suggests that temperature does not have a strong influence on the notch effect at the studied range of temperatures and notch radii. The values of the derived critical distances (L) are collected in Table 7, considering either the calculated curves or the best-fit curves. These values are compared with those previously obtained by the authors (Justo et al. 2020) using four-point bending tests. In general, the results are consistent and no clear trends with temperature are observed. This is because both the tensile strength and the fracture toughness increase in a similar proportion from 23°C to 250°C (see Tables 4 and 6). Thus, based on Eq. (1), the value of L should not present significant variations if K_{IC}/σ_u is roughly constant at both temperatures.

For a clearer comparison between the results of the three-point bending tests performed in this work and those performed under four-point bending conditions in a previous research (Justo et al. 2020), Fig. 14 displays, together in the same plot, the average K_{IN} values for each notch radius, for both loading types and both at 23°C and 250°C. It is directly observed that both methods are in very good agreement at the two considered temperatures. The main difference between both loading types is the distribution of shear and bending stresses. Assuming centred loads, four-point bending tests ensure a constant bending moment and no shear stresses between the inner loading points, while in three-point bending tests, pure mode I conditions are only achieved along the notch bisector. In any case, both methodologies have proven to offer consistent and very similar results.

On the other hand, dealing with the numerical approach, this is based on the direct application of the LM expression defined by Eq. (2) on the critical plane, which, in the case of pure mode I loading conditions, corresponds to the bisector of the notch. This way, one value of L is derived for each notch simply by finding the distance at which failure criterion defined by the LM is fulfilled (Eq. (2)). Table 8 gathers the obtained critical distances (L) for each case.

Thus, the mean critical distance for the Moleanos limestone at 23°C is 2.8 mm while at 250°C L slightly increases to 3.0 mm. The numerically obtained values of L are lower than those obtained analytically for the same mode I loading conditions (Table 7). However, despite these differences, both the analytical and the numerical approach offer similar and relatively accurate predictions according to Fig. 15.

Fig. 15 represents the ratio between the predicted and the experimentally obtained failure load (F_{TCD}/F_{EXP}) against the notch radii of the specimens. The dots correspond to the failure load prediction of each of the individual tests according to the Eq. (7) and the black solid line represents the mean predictions considering the same criterion. These analytical results have been obtained using the calculated value of L collected in Table 7. By contrast, the grey solid line stands for the numerically obtained fracture predictions, for which the mean value of L (Table 8) has been considered at each temperature. The horizontal red dotted lines define an error interval of $\pm 20\%$, which is a common range in fracture mechanics to define a boundary of good accuracy predictions. Systematic applications of the TCD were seen to return predictions typically falling within an error interval of $\pm 20\%$ (Taylor 2007). In general terms, the obtained predictions fall within the error interval of $\pm 20\%$, although the individual test results performed at 250°C show a significantly higher scatter compared to those at 23°C.

Both the analytical and the numerical approaches are based on the application of the LM failure criterion defined by Eq. (2) along the bisector of the notches. However, it can be observed that despite the differences in the values of L in both approaches, the failure load predictions are relatively similar. This is caused by the fact that different stress distributions are being considered in each case. The analytical approach considers the stress distribution of Creager and Paris (1967) while the numerical approach considers the stresses of the performed linear-elastic analyses. This is what generates the observed differences in the L values, although both approaches have been shown to be valid. Even the analytical solution based on Eq. (3) offers accurate load failure predictions for the largest notches beyond its application range.

4.3. Interpretation of mixed mode I+II results

With regards to the mixed mode I+II results, the performed numerical analyses follow the same procedure as that described for mode I loading conditions, with the only difference that the critical plane over which Eq. (2) is assessed changes.

Once the values of M_e are known for each test configuration (Table 3), the variation of the critical distance (L) with M_e can be analysed, obtaining the values of L by rescaling the stress-distance curves as above. Fig. 16 represent the critical distance versus the mode mixity both for 23°C and 250°C. Similar trends are observed in both cases, although the critical distance values are slightly higher at 250°C. According to Eq. (14), there is a linear relation between L and M_e . For this reason, the obtained points have been adjusted with a linear equation as those indicated in Fig. 3, which seems to indicate that L slightly decreases with M_e at the studied range of mode mixities with predominant mode I influence.

However, in order to study the observed tendency in more detail, Fig. 17 represents the same results depicted in Fig. 16 but distinguishing the values according to the notch radii (ρ), using a different symbol for each one. When the results of each notch radius are analysed separately, it seems that the values of the critical distance are roughly constant for each notch radius or, at least, no clear decreasing or increasing tendencies are observed. In general terms, L seems to increase with the notch radius both at 23°C and at 250°C. This generality can also be observed in those L values collected in Table 8 for those models subjected to mode I loading ($M_e = 1$).

The variation of the critical distance with the notch radius is clearly depicted in Fig. 18. The horizontal axis represents the square root of ρ for the sake of clarity of the results. In any case, the increasing trend of L with notch radius seems to be clear both at 23°C and at 250°C.

With all this, the observed results indicate that L somehow increases with the notch radius rather than decreasing with M_e for the cases studied here. Thus, based on the obtained results, it seems that L is not sensitive to the mode mixity and, as a material constant characteristic parameter, the value of the critical distance seems to be independent from the mode I and II mixity at the studied range of values. However, further research is needed for other cases. Establishing a real definition of the physical meaning of the critical distance is still a fundamental challenge among researchers (Taylor 2017). L is supposed to be an intrinsic parameter of the material and has been related by different authors to clearly identifiable microstructural distances such as the grain size in the case of rocks (e.g., Justo et al. 2017; Taylor 2017). The analytical expressions corresponding to TCD do not consider the possible influence of the notch radius on the critical distance, assuming it is a material property (Eq. (1)). However, the results shown in this article seem to show a certain influence on ρ . Dealing

with this topic, Pluinage and Capelle (2014) studied several characteristic length parameters generally used in different notch fracture criteria and stated that the scale length of the fracture volume process is not intrinsic to material but depends on the notch geometry, loading mode, constraints, etc. All this being said, it should be kept in mind that the observed variations of L do not have significant effects when performing predictions of critical loads.

5. CONCLUSIONS

This work studies the fracture behaviour of a Moleanos limestone with U-shaped notches, subjected to mixed mode (I+II) loading conditions and to different temperatures by means of the Theory of Critical Distances. The performed fracture assessments are based on an exhaustive laboratory campaign comprising 30 tensile splitting (Brazilian) tests and almost 400 three-point bending tests on SENB specimen with notch radii varying from 0.15 mm up to 15 mm and with four different loading positions, all of them at 23°C and at 250°C. These test configurations allow opening-sliding shear mixed mode (I+II) fracture conditions with predominant mode I influence to be analysed.

The interpretation of the results is performed according to the LM of the TCD, which states that failure occurs when the average stress over a distance equal to two times the critical distance (L) reaches the tensile strength of the rock. This failure criterion is assessed along a critical plane starting at the notch, which is equal to the bisector plane for mode I loading conditions but presents a rotation according to the mode II influence.

Several conclusions should be highlighted from the obtained results. First, the direct observation of the test outcomes shows an increment of the tensile strength of the Moleanos limestone from 23°C to 250°C, and an increment of the load-bearing capacity of the SENB specimens with both the eccentricity of the load (higher mode II influence) and the notch radius. Besides, the linear elastic quasi-brittle behaviour of the Moleanos limestone has been observed even at 250°C, which allows the use of LEFM on which the TCD is based.

The considered analytical and numerical approaches for the fracture assessment of mode I loaded rocks offer similar and accurate failure load predictions within an error interval of $\pm 20\%$ for the whole range of analysed notch radii and temperatures, even though certain differences are observed in the obtained values of the critical distance. Proceeding along similar tracks, the interpretation of the mixed mode (I+II) results allows the critical distance for different mode mixities (M_e) to be characterised using the stress field at the corresponding critical plane derived from the numerical models. When analysing the obtained values of L against M_e , a linear relation can be interpreted. However, if these results are observed separately for each notch radius, a certain influence of the notch radius on the critical distance is shown. This influence seems to indicate that L is relatively constant with M_e for each notch radius for the studied cases.

Thus, the application of TCD has proven to be an appropriate tool in these cases to perform fracture assessments of U-notched rock components with relatively large notch radii under mixed mode (I+II) loading conditions, even at high temperatures as long as linear elastic conditions are guaranteed.

ACKNOWLEDGEMENTS

The authors of this work would like to express their gratitude to the Spanish Ministry of Economy and Competitiveness and to the European Regional Development Fund (ERDF) for financing the National Plan Project (Ref.: BIA2015-67479-R) under the name of “The Critical Distance in Rock Fracture”, as well as to the Department of Universities and Research, Environment and Social Policy of the Government of Cantabria, for financing the Project “Characterisation of the fracture process in rocks for geothermal applications”. The authors would also like to thank J. de la Fuente and E. Gútiez, technicians in the Geotechnical Research Group for their help with the laboratory work.

CONFLICT OF INTEREST

The authors of this work declare that they have no conflict of interest.

REFERENCES

Akbardoost J, Ayatollahi MR, Aliha MRM, Pavier MJ, Smith DJ (2014) Size-dependent fracture behavior of Guiting limestone under mixed mode loading. *Int J Rock Mech Min Sci* 71:369-380.

Aliha MRM, Ayatollahi MR (2013) Two-parameter fracture analysis of SCB rock specimen under mixed mode loading. *Eng Fract Mech* 103:115-123.

Aliha MRM, Ayatollahi MR, Kharrazi B (2009) Mode II brittle fracture assessment using ASFPB specimen. *Int J Fract* 159:241-246.

Aliha MRM, Ayatollahi MR, Smith DJ, Pavier MJ (2010) Geometry and size effects on fracture trajectory in a limestone rock under mixed mode loading. *Eng Fract Mech* 77:2200-2212.

Aliha MRM, Berto F, Mousavi A, Razavi SMJ (2017) On the applicability of ASED criterion for predicting mixed mode I+II fracture toughness results of a rock material. *Theor Appl Fract Mech* 92:198-204.

Aliha MRM, Hosseinpour GR, Ayatollahi MR (2013) Application of cracked triangular specimen subjected to three-point bending for investigating fracture behavior of rock materials. *Rock Mech Rock Eng* 46:1023-1034.

Aliha MRM, Mousavi SS, Ghoreishi SMN (2019) Fracture load prediction under mixed mode I+II using a stress based method for brittle materials tested with the asymmetric four-point bend specimen. *Theor Appl Fract Mech* 103:102249.

Aliha MRM, Mousavi SS (2020) Sub-sized short bend beam configuration for the study of mixed mode fracture. *Eng Fract Mech* 225:106830.

Aliha MRM, Sistaninia M, Smith DJ, Pavier MJ, Ayatollahi MR (2012) Geometry effects and statistic analysis of mode I fracture in Guiting limestone. *Int J Rock Mech Min Sci* 51:128-135.

Al-Shayea N, Khan K, Abduljawwad S (2000) Effects of confining pressure and temperature on mixed-mode (I-II) fracture toughness of a limestone rock. *Int J Rock Mech Min Sci* 37:629-643.

Anderson TL (2005) *Fracture Mechanics: Fundamentals and Applications*. CRC Press, Florida .

ASTM D3967-16 (2016) *Standard Test Method for Splitting Tensile Strength of Intact Rock Core Specimens*. West Conshohocken, PA: ASTM International.

Ayatollahi MR, Aliha MRM (2008) On the use of Brazilian disc specimen for calculating mixed mode I-II fracture toughness of rock materials. *Eng Fract Mech* 75:4631-4641.

Ayatollahi MR, Torabi AR (2009) A criterion for brittle fracture in U-notched components under mixed-mode loading. *Engng Fract Mech* 76:1883-1896.

Bahmani A, Aliha MRM, Jebalbarez Sarbijan M, Mousavi SS (2020) An extended edge-notch disc bend (ENDB) specimen for mixed-mode I+II fracture assessments. *Int J Solid Struct* 193:239-250.

Barenblatt GI (1962) The mathematical theory of equilibrium of cracks in brittle fracture. *Adv Appl Mech* 7:55–129.

Berto F, Lazzarin P, Gómez FJ, Elices M (2007) Fracture assessment of U-notches under mixed mode loading: two procedures based on the equivalent local mode I concept. *Int J Fract* 148:415–433.

Brinkgreve RBJ, Engin E, WM Swolfs WM (2017) *Plaxis 2D Manual 2017*. The Netherlands.

Carpinteri A (1987) Stress-singularity and generalised fracture toughness at the vertex of re-entrant corners. *Engng Fract Mech* 26:143–55.

Cicero S, García T, Castro J, Madrazo V, Andrés D (2014) Analysis of notch effect on the fracture behaviour of granite and limestone: An approach from the Theory of Critical Distances. *Eng Geol* 177:1-9.

Cornetti P, Sapora A, Carpinteri A (2016) Short cracks and V-notches: finite fracture mechanics vs. cohesive crack model. *Eng Fract Mech* 168:2–12.

Creager M, Paris C (1967) Elastic field equations for blunt cracks with reference to stress corrosion cracking. *Int J Fract* 3:247-252.

Dugdale DS (1960) Yielding of steel sheets containing slits. *J Mech Phys Solids* 8:100–108.

Dunn ML, Suwito W, Cunningham SJ (1997) Fracture initiation at sharp notches: correlation using critical stress intensities. *Int J of Solids and Structures* 34:3873–83.

Dunn ML, Suwito W, Cunningham SJ, May CW (1997b) Fracture initiation at sharp notches under mode I, mode II, and mild mixed mode loading. *Int J Fract* 84:367–81.

EN 12372:2006 (2006) *Natural stone test methods - determination of flexural strength under concentrated load*. European Committee for Standardization.

Erdogan F, Sih CG (1963) On the crack extension in plates under plane loading and transverse shear. *J Basic Eng* 85:519-525.

Filippi S, Lazzarin P, Tovo R (2002) Developments of some explicit formulas useful to describe elastic stress field ahead of the notches. *Int J Solids Struct* 39:4543–4565.

Folk RL (1959) Practical petrographic classification of limestones. *Bull Am Assoc Perol Geol* 43(1):1-38.

Gómez FJ, Elices M (2003) A fracture criterion for sharp V-notched samples. *Int J Fract* 123:163-75.

Gómez FJ, Elices M, Berto F, Lazzarin P (2007) Local strain energy to assess the static failure of U-notches in plates under mixed mode loading. *Int J Fract* 145:29–45.

Gómez FJ, Elices M, Valiente A (2000) Cracking in PMMA containing U-shaped notches. *Fatigue Fract Eng Mater* 23:795–803.

Gómez FJ, Guinea G, Elices M (2006) Failure criteria for linear elastic materials with U-notches. *Int J Fract* 141:99-113.

Gross R, Mendelson A (1972) Plane elastostatic analysis of V-notched plates. *Int J Fract Mech* 8:267–276.

Justo J, Castro J (2021) Mechanical properties of 4 rocks at different temperatures and fracture assessment using the Strain Energy Density criterion. *Geomech Energy Envir* 25:100212.

Justo J, Castro J, Cicero S (2018) Energy-based approach for fracture assessment of several rocks containing U-shaped notches through the application of the SED criterion. *Int J Rock Mech Min Sci* 110:306-315.

Justo J, Castro J, Cicero S (2020) Notch effect and fracture load predictions of rock beams at different temperatures using the Theory of Critical Distances. *Int J Rock Mech Min Sci* 125:104161.

Justo J, Castro J, Cicero S, Sánchez-Carro MA, Husillos R (2017) Notch effect on the fracture of several rocks: Application of the Theory of the Critical Distances. *Theor Appl Fract Mech* 90:251-258.

Lazzarin P, Filippi S (2006) A generalized stress intensity factor to be applied to rounded V-shaped notches. *Int J Solids Struct* 43:2461–2478.

Lazzarin P, Zambardi R (2001) A finite-volume-energy based approach to predict the static and fatigue behavior of components with sharp V-shaped notches. *Int J Fract* 112(3):275–298.

Louks R, Askes H, Susmel L (2016) A generalised approach to rapid finite element design of notched materials against static loading using the Theory of Critical Distances. *Mater Design* 108:769-779.

Mirsayar MM, Razmi A, Aliha MRM, Berto F (2018) EMTSN criterion for evaluating mixed mode I/II crack propagation in rock materials. *Eng Fract Mech* 190:186-197.

Negru R, Marsavina L, Voiconi T, Linul E, Filipescu H, Belgiu G (2015) Application of the TCD for brittle fracture of notched PUR materials. *Theor Appl Fract Mech* 80:87-95.

Nejati M, Aminzadeh A, Driesner T, Saar MO (2020) On the directional dependency of Mode I fracture toughness in anisotropic rocks. *Theor Appl Fract Mech* 107:102494.

Neuber H (1958) Theory of notch stresses. Springer-Verlag, Berlin.

Nui LS, Chehimi C, Pluvinage G (1994) Stress field near a large blunted tip V-notch and application of the concept of the critical notch stress intensity factor (NSIF) to the fracture toughness of very brittle materials. *Engng Fract Mech* 49:325–35.

Mousavi SS, Aliha MRM, Imani DM (2020) On the use of edge cracked short bend beam specimen for PMMA fracture toughness testing under mixed-mode I/II. *Polym test* 81:106199.

Peterson RE (1959) Notch Sensitivity. McGraw Hill, New York.

Pluvinage G, Capelle J (2014) On characteristic lengths used in notch fracture mechanics. *Int J Fract* 187:187-197.

Radaj D, Lazzarin P, Berto F (2013) Generalised Neuber concept of fictitious notch rounding. *Int J Fatigue* 51:105–115.

Ramspott LD, Ballou LB, Carlson RC, et al. (1979) Technical concept for a test of geologic storage of spent reactor fuel in the climax granite, Nevada Test Site. California Univ., Livermore, Lawrence Livermore Lab. United States.

Ranjith PG, Viete DR, Chen BJ, Perera MSA (2012) Transformation plasticity and the effect of temperature on the mechanical behaviour of hawkesbury sandstone at atmospheric pressure. *Eng Geol* 151(151):120–127.

Sangsefidi M, Akbardoost J, Mesbah M (2020) Experimental and theoretical fracture assessment of rock-type U-notched specimens under mixed mode I/II loading. *Eng Fract Mech* 230:106990.

Seweryn A (1994) Brittle fracture criterion for structures with sharp notches. *Engng Fract Mech* 47:673–81.

Seweryn A, Poskrobko S, Mroz Z (1997) Brittle fracture in plane elements with sharp notches under mixed-mode loading. *J Engng Mech ASCE* 123(6):535–43.

Sheppard SD (1991) Field effects in fatigue crack initiation: long life fatigue strength. *J Mech Des (ASME)* 113:118–194.

Susmel L, Taylor D (2008) The theory of critical distances to predict static strength of notched brittle components subjected to mixed-mode loading. *Eng Fract Mech* 75:534-550.

Tanaka K (1983) Engineering formulae for fatigue strength reduction to crack-like notches. *Int J Fract* 22:R39–R45.

Taylor D (2004) Predicting the fracture strength of ceramic materials using the theory of critical distances. *Eng Fract Mech* 71:2407–16.

Taylor D (2006) The theory of critical distances applied to the prediction of brittle fracture in metallic materials. *Struct Integrity Durability* 1:145–54.

Taylor D (2007) *The Theory of Critical Distances: a new perspective in fracture mechanics*. Elsevier, London.

Taylor D (2017) *The Theory of Critical Distances: A link to micromechanisms*. *Theor Appl Fract Mech* 90:228-233.

Taylor D, Merlo M, Pegley R, Cavatorta MP (2004) The effect of stress concentrations on the fracture strength of polymethylmethacrylate. *Mat Sci Eng A*382:288–94.

Vargiu F, Sweeney D, Firrao D, Matteis P, Taylor D (2017) Implementation of the Theory of Critical Distances using mesh control. *Theor Appl Fract Mech* 92:113-121.

Williams ML (1952) Stress singularities resulting from various boundary conditions in angular corners of plates in extension. *J Appl Mech* 19:526–528.

Xeidakis GS, Samaras IS, Zacharopoulos DA, Papakalitakis GE (1996) Crack growth in a mixed-mode loading on marble beams under three point bending. *Int J Fract* 79:197-208.

APPENDIX A

Table 9 collects the individual results of the performed three-point bending tests.

LIST OF FIGURES

Fig. 1.- Petrographic image of the Moleanos limestone (4x, crossed Nicol)

Fig. 2.- Schematic representation of the (a) Brazilian tests and (b) Three-point bending tests.

Fig. 3.- Experimental setup of the (a) Brazilian tests, (b) Three-point bending tests and (c) heat chamber coupled to the hydraulic press.

Fig. 4.- Tested SENB samples with different notch radii.

Fig. 5.- Schematic representation of the LM criterion applied on the stress law in the bisector of the notch.

Fig. 6.- Example of a finite element model with the refined region to simulate three-point bending tests ($P1$, $\rho = 1$ mm).

Fig. 7.- Polar coordinate system in U-shaped notches.

Fig. 8.- NSIFs versus distance for different notch radii ($\rho = 1, 4$ and 15 mm) and loading positions ($m = 0$ and 12 mm) at room temperature.

Fig. 9.- Schematic representation of the critical plane and stress-distance curves under (a) mode I and (b) mode I+II loading conditions.

Fig. 10.- Numerically obtained critical planes and stress-distance curves for two different models with $\rho = 1$ mm and (a) $m = 0$ mm and (b) $m = 12$ mm, both of them at room temperature.

Fig. 11.- Load-displacement curves of the three-point bending tests for different notch radii ($\rho = 0.15, 2, 7$ and 15 mm) and loading positions ($m = 0$ and 12 mm), both for 23°C and 250°C .

Fig. 12.- Some representative fractured SENB specimens for each loading position and different notch radii ($\rho = 0.15, 1, 7$ and 15 mm), obtained from three-point bending tests at 23°C and 250°C . In all cases the load is applied to the left of the notch.

Fig. 13.- Apparent fracture toughness (K_{IN}) versus square root of the notch radius and comparison with the LM of the TCD for both 23°C and 250°C .

Fig. 14.- Comparison between mean K_{IN} values of the Moleanos limestone obtained from three-point bending and four-point bending (Justo et al. 2020) tests, both at 23°C and at 250°C .

Fig. 15.- Load fracture predictions of the mode I loaded three-point bending tests obtained from the analytical and the numerical analyses according to the LM of the TCD.

Fig. 16.- Variation of the critical distance (L) with the mode mixity (M_e) at 23°C and 250°C .

Fig. 17.- Variation of the critical distance (L) with the mode mixity (M_e) at 23°C and 250°C , represented with a different symbol for each notch radius.

Fig. 18.- Variation of the critical distance (L) with the square root of the notch radius ($\rho^{1/2}$) at 23°C and 250°C .

LIST OF TABLES

Table 1.- Summary of the three-point bending test variables.

Table 2.- Mean values of the Young's modulus and Poisson's ratio of the Moleanos limestone at room temperature and at 250°C (Justo et al. 2021).

Table 3.- Calculated values of the mode mixity (M_e) for each numerical model according to Eq. (8).

Table 4.- Tensile strength and standard deviation of the Moleanos limestone at 23°C and 250°C.

Table 5.- Average failure loads ($F_{E,exp}$) for each three-point bending test configuration at 23°C and 250°C.

Table 6.- Fracture toughness and standard deviation of the Moleanos limestone at 23°C and 250°C.

Table 7.- Summary of the calculated and best-fit values of the critical distance (L).

Table 8.- Numerically obtained critical distances (L) for each model.

Table 9.- Experimentally obtained failure loads in the performed three-point bending tests.

LIST OF TABLES

Table 10.- Summary of the three-point bending test variables.

Temperature	m (mm)	ρ (mm)	Repetitiveness
23°C (T1)	0 (P1)	0.15	1
		0.5	2
	4 (P2)	1	3
		2	4
250°C (T2)	8 (P3)	4	5
		7	6
	12 (P4)	10	
		15	

Table 11.- Mean values of the Young's modulus and Poisson's ratio of the Moleanos limestone at room temperature and at 250°C (Justo et al. 2021).

	23°C	250°C
Young's modulus, E_{50} (GPa)	38.4	49.2
Poisson's ratio, ν	0.31	0.28

Table 12.- Calculated values of the mode mixity (M_e) for each numerical model according to Eq. (8).

ρ (mm)	23°C				250°C			
	P1	P2	P3	P4	P1	P2	P3	P4
0.15	1.000	0.955	0.945	0.928	1.000	0.967	0.948	0.892
0.5	1.000	0.972	0.935	0.923	1.000	0.960	0.935	0.934
1	1.000	0.965	0.937	0.922	1.000	0.957	0.928	0.913
2	1.000	0.953	0.921	0.904	1.000	0.952	0.920	0.904
4	1.000	0.930	0.890	0.881	1.000	0.934	0.894	0.880
7	1.000	0.911	0.866	0.853	1.000	0.911	0.850	0.853
10	1.000	0.890	0.837	0.827	1.000	0.890	0.837	0.827
15	1.000	0.856	0.792	0.781	1.000	0.856	0.792	0.783

Table 13.- Tensile strength and standard deviation of the Moleanos limestone at 23°C and 250°C.

Moleanos limestone	
Tensile strength (σ_u) – 23°C	$6.9 \pm 1.2^*$ MPa
Tensile strength (σ_u) – 250°C	$8.9 \pm 0.5^*$ MPa

*Standard deviation

Table 14.- Average failure loads (F_{Exp}) for each three-point bending test configuration at 23°C and 250°C.

Temp. (°C)	ρ (mm)	P1	P2	P3	P4
23°C	0.15	320 N	311 N	347 N	385 N
	0.5	289 N	299 N	295 N	337 N
	1	338 N	341 N	340 N	352 N
	2	383 N	368 N	371 N	405 N
	4	329 N	346 N	323 N	352 N
	7	346 N	332 N	346 N	396 N
	10	323 N	335 N	313 N	319 N
	15	355 N	348 N	375 N	389 N
250°C	0.15	406 N	435 N	521 N	526 N
	0.5	364 N	346 N	440 N	565 N
	1	456 N	447 N	493 N	535 N
	2	511 N	474 N	542 N	530 N
	4	521 N	429 N	513 N	549 N
	7	461 N	517 N	489 N	492 N
	10	490 N	470 N	482 N	506 N
	15	518 N	461 N	467 N	557 N

Table 15.- Fracture toughness and standard deviation of the Moleanos limestone at 23°C and 250°C.

	Three-point bending	Four-point bending (Justo et al. 2020)
Fracture toughness (K_{IC}) – 23°C	$0.77 \pm 0.05^*$ MPa·m ^{1/2}	$0.73 \pm 0.11^*$ MPa·m ^{1/2}
Fracture toughness (K_{IC}) – 250°C	$1.02 \pm 0.15^*$ MPa·m ^{1/2}	$1.07 \pm 0.17^*$ MPa·m ^{1/2}

*Standard deviation

Table 16.- Summary of the calculated and best-fit values of the critical distance (L).

	Three-point bending	Four-point bending (Justo et al. 2020)
Best-fit value of L – 23°C	7.4 mm	4.0 mm
Calculated value of L – 23°C	4.0 mm	4.0 mm
Best-fit value of L – 250°C	3.9 mm	7.4 mm
Calculated value of L – 250°C	4.2 mm	4.8 mm

Table 17.- Numerically obtained critical distances (L) for each model.

ρ (mm)	23°C	250°C
0.15	2.5 mm	2.6 mm
0.5	2.5 mm	2.4 mm
1	2.6 mm	2.8 mm
2	2.8 mm	3.0 mm
4	2.8 mm	3.2 mm
7	3.0 mm	3.2 mm
10	2.7 mm	3.3 mm
15	3.1 mm	3.6 mm

Table 18.- Experimentally obtained failure loads in the performed three-point bending tests.

Test code	Failure load, F (N)						
T1-P1-0.15-1	322	T1-P2-0.15-1	328	T1-P3-0.15-1	411	T1-P4-0.15-1	400
T1-P1-0.15-2	282	T1-P2-0.15-2	290	T1-P3-0.15-2	370	T1-P4-0.15-2	356
T1-P1-0.15-3	342	T1-P2-0.15-3	313	T1-P3-0.15-3	303	T1-P4-0.15-3	365
T1-P1-0.15-4	300	T1-P2-0.15-4	333	T1-P3-0.15-4	389	T1-P4-0.15-4	404
T1-P1-0.15-5	311	T1-P2-0.15-5	264	T1-P3-0.15-5	292	T1-P4-0.15-5	407
T1-P1-0.15-6	364	T1-P2-0.15-6	340	T1-P3-0.15-6	318	T1-P4-0.15-6	375
T1-P1-0.5-1	318	T1-P2-0.5-1	298	T1-P3-0.5-1	301	T1-P4-0.5-1	400
T1-P1-0.5-2	296	T1-P2-0.5-2	282	T1-P3-0.5-2	301	T1-P4-0.5-2	309
T1-P1-0.5-3	262	T1-P2-0.5-3	300	T1-P3-0.5-3	287	T1-P4-0.5-3	345
T1-P1-0.5-4	295	T1-P2-0.5-4	311	T1-P3-0.5-4	298	T1-P4-0.5-4	305
T1-P1-0.5-5	292	T1-P2-0.5-5	300	T1-P3-0.5-5	286	T1-P4-0.5-5	318
T1-P1-0.5-6	268	T1-P2-0.5-6	303	T1-P3-0.5-6	298	T1-P4-0.5-6	343
T1-P1-1-1	316	T1-P2-1-1	372	T1-P3-1-1	353	T1-P4-1-1	353
T1-P1-1-2	389	T1-P2-1-2	346	T1-P3-1-2	266	T1-P4-1-2	214
T1-P1-1-3	339	T1-P2-1-3	347	T1-P3-1-3	373	T1-P4-1-3	345
T1-P1-1-4	341	T1-P2-1-4	351	T1-P3-1-4	311	T1-P4-1-4	434
T1-P1-1-5	338	T1-P2-1-5	314	T1-P3-1-5	415	T1-P4-1-5	392
T1-P1-1-6	303	T1-P2-1-6	314	T1-P3-1-6	323	T1-P4-1-6	372
T1-P1-2-1	409	T1-P2-2-1	387	T1-P3-2-1	391	T1-P4-2-1	333
T1-P1-2-2	362	T1-P2-2-2	349	T1-P3-2-2	373	T1-P4-2-2	403
T1-P1-2-3	395	T1-P2-2-3	364	T1-P3-2-3	369	T1-P4-2-3	410
T1-P1-2-4	400	T1-P2-2-4	400	T1-P3-2-4	378	T1-P4-2-4	458
T1-P1-2-5	334	T1-P2-2-5	356	T1-P3-2-5	370	T1-P4-2-5	404
T1-P1-2-6	397	T1-P2-2-6	351	T1-P3-2-6	342	T1-P4-2-6	419
T1-P1-4-1	317	T1-P2-4-1	314	T1-P3-4-1	326	T1-P4-4-1	368
T1-P1-4-2	336	T1-P2-4-2	347	T1-P3-4-2	296	T1-P4-4-2	345
T1-P1-4-3	311	T1-P2-4-3	345	T1-P3-4-3	341	T1-P4-4-3	370
T1-P1-4-4	382	T1-P2-4-4	337	T1-P3-4-4	334	T1-P4-4-4	343
T1-P1-4-5	289	T1-P2-4-5	350	T1-P3-4-5	328	T1-P4-4-5	310
T1-P1-4-6	338	T1-P2-4-6	382	T1-P3-4-6	314	T1-P4-4-6	373
T1-P1-7-1	340	T1-P2-7-1	327	T1-P3-7-1	387	T1-P4-7-1	319

T1-P1-7-2	360	T1-P2-7-2	309	T1-P3-7-2	348	T1-P4-7-2	426
T1-P1-7-3	332	T1-P2-7-3	268	T1-P3-7-3	376	T1-P4-7-3	443
T1-P1-7-4	330	T1-P2-7-4	363	T1-P3-7-4	353	T1-P4-7-4	415
T1-P1-7-5	364	T1-P2-7-5	361	T1-P3-7-5	347	T1-P4-7-5	377
T1-P1-7-6	352	T1-P2-7-6	361	T1-P3-7-6	263	T1-P4-7-6	396
T1-P1-10-1	302	T1-P2-10-1	308	T1-P3-10-1	295	T1-P4-10-1	299
T1-P1-10-2	294	T1-P2-10-2	316	T1-P3-10-2	305	T1-P4-10-2	350
T1-P1-10-3	340	T1-P2-10-3	326	T1-P3-10-3	358	T1-P4-10-3	276
T1-P1-10-4	358	T1-P2-10-4	335	T1-P3-10-4	295	T1-P4-10-4	331
T1-P1-10-5	330	T1-P2-10-5	333	T1-P3-10-5	320	T1-P4-10-5	343
T1-P1-10-6	311	T1-P2-10-6	390	T1-P3-10-6	303	T1-P4-10-6	313
T1-P1-15-1	350	T1-P2-15-1	361	T1-P3-15-1	358	T1-P4-15-1	395
T1-P1-15-2	354	T1-P2-15-2	398	T1-P3-15-2	384	T1-P4-15-2	381
T1-P1-15-3	341	T1-P2-15-3	375	T1-P3-15-3	372	T1-P4-15-3	391
T1-P1-15-4	362	T1-P2-15-4	270	T1-P3-15-4	352	T1-P4-15-4	383
T1-P1-15-5	361	T1-P2-15-5	323	T1-P3-15-5	389	T1-P4-15-5	397
T1-P1-15-6	359	T1-P2-15-6	362	T1-P3-15-6	395	T1-P4-15-6	385
T2-P1-0.15-1	307	T2-P2-0.15-1	416	T2-P3-0.15-1	472	T2-P4-0.15-1	505
T2-P1-0.15-2	435	T2-P2-0.15-2	357	T2-P3-0.15-2	542	T2-P4-0.15-2	566
T2-P1-0.15-3	426	T2-P2-0.15-3	441	T2-P3-0.15-3	591	T2-P4-0.15-3	555
T2-P1-0.15-4	469	T2-P2-0.15-4	469	T2-P3-0.15-4	509	T2-P4-0.15-4	622
T2-P1-0.15-5	431	T2-P2-0.15-5	446	T2-P3-0.15-5	530	T2-P4-0.15-5	427
T2-P1-0.15-6	368	T2-P2-0.15-6	483	T2-P3-0.15-6	480	T2-P4-0.15-6	480
T2-P1-0.5-1	475	T2-P2-0.5-1	384	T2-P3-0.5-1	437	T2-P4-0.5-1	637
T2-P1-0.5-2	413	T2-P2-0.5-2	376	T2-P3-0.5-2	442	T2-P4-0.5-2	615
T2-P1-0.5-3	390	T2-P2-0.5-3	247	T2-P3-0.5-3	487	T2-P4-0.5-3	581
T2-P1-0.5-4	347	T2-P2-0.5-4	240	T2-P3-0.5-4	345	T2-P4-0.5-4	487
T2-P1-0.5-5	307	T2-P2-0.5-5	418	T2-P3-0.5-5	451	T2-P4-0.5-5	520
T2-P1-0.5-6	251	T2-P2-0.5-6	408	T2-P3-0.5-6	475	T2-P4-0.5-6	551
T2-P1-1-1	375	T2-P2-1-1	-	T2-P3-1-1	477	T2-P4-1-1	484
T2-P1-1-2	389	T2-P2-1-2	491	T2-P3-1-2	484	T2-P4-1-2	541
T2-P1-1-3	501	T2-P2-1-3	399	T2-P3-1-3	470	T2-P4-1-3	546
T2-P1-1-4	411	T2-P2-1-4	501	T2-P3-1-4	493	T2-P4-1-4	587
T2-P1-1-5	521	T2-P2-1-5	398	T2-P3-1-5	546	T2-P4-1-5	503
T2-P1-1-6	538	T2-P2-1-6	444	T2-P3-1-6	485	T2-P4-1-6	547
T2-P1-2-1	515	T2-P2-2-1	427	T2-P3-2-1	629	T2-P4-2-1	516
T2-P1-2-2	548	T2-P2-2-2	451	T2-P3-2-2	507	T2-P4-2-2	507
T2-P1-2-3	482	T2-P2-2-3	438	T2-P3-2-3	-	T2-P4-2-3	-
T2-P1-2-4	467	T2-P2-2-4	545	T2-P3-2-4	596	T2-P4-2-4	562
T2-P1-2-5	575	T2-P2-2-5	508	T2-P3-2-5	393	T2-P4-2-5	491
T2-P1-2-6	477	T2-P2-2-6	474	T2-P3-2-6	585	T2-P4-2-6	576
T2-P1-4-1	471	T2-P2-4-1	344	T2-P3-4-1	442	T2-P4-4-1	523
T2-P1-4-2	398	T2-P2-4-2	325	T2-P3-4-2	511	T2-P4-4-2	582
T2-P1-4-3	641	T2-P2-4-3	542	T2-P3-4-3	463	T2-P4-4-3	-
T2-P1-4-4	555	T2-P2-4-4	449	T2-P3-4-4	568	T2-P4-4-4	545

T2-P1-4-5	563	T2-P2-4-5	610	T2-P3-4-5	573	T2-P4-4-5	593
T2-P1-4-6	498	T2-P2-4-6	304	T2-P3-4-6	519	T2-P4-4-6	503
T2-P1-7-1	536	T2-P2-7-1	556	T2-P3-7-1	472	T2-P4-7-1	483
T2-P1-7-2	461	T2-P2-7-2	450	T2-P3-7-2	483	T2-P4-7-2	498
T2-P1-7-3	447	T2-P2-7-3	602	T2-P3-7-3	352	T2-P4-7-3	474
T2-P1-7-4	433	T2-P2-7-4	576	T2-P3-7-4	468	T2-P4-7-4	484
T2-P1-7-5	520	T2-P2-7-5	430	T2-P3-7-5	566	T2-P4-7-5	519
T2-P1-7-6	371	T2-P2-7-6	490	T2-P3-7-6	595	T2-P4-7-6	495
T2-P1-10-1	571	T2-P2-10-1	477	T2-P3-10-1	547	T2-P4-10-1	594
T2-P1-10-2	466	T2-P2-10-2	504	T2-P3-10-2	495	T2-P4-10-2	365
T2-P1-10-3	471	T2-P2-10-3	596	T2-P3-10-3	387	T2-P4-10-3	534
T2-P1-10-4	327	T2-P2-10-4	369	T2-P3-10-4	487	T2-P4-10-4	582
T2-P1-10-5	616	T2-P2-10-5	409	T2-P3-10-5	564	T2-P4-10-5	521
T2-P1-10-6	489	T2-P2-10-6	463	T2-P3-10-6	414	T2-P4-10-6	440
T2-P1-15-1	577	T2-P2-15-1	387	T2-P3-15-1	361	T2-P4-15-1	446
T2-P1-15-2	-	T2-P2-15-2	500	T2-P3-15-2	423	T2-P4-15-2	735
T2-P1-15-3	565	T2-P2-15-3	369	T2-P3-15-3	464	T2-P4-15-3	599
T2-P1-15-4	420	T2-P2-15-4	468	T2-P3-15-4	471	T2-P4-15-4	573
T2-P1-15-5	508	T2-P2-15-5	529	T2-P3-15-5	549	T2-P4-15-5	397
T2-P1-15-6	-	T2-P2-15-6	512	T2-P3-15-6	531	T2-P4-15-6	594

LIST OF FIGURES

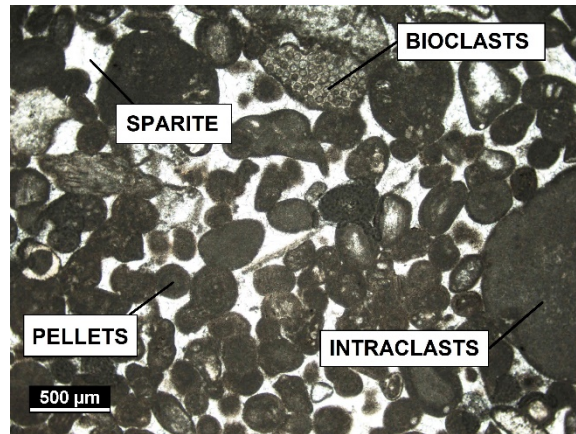


Fig. 1.- Petrographic image of the Moleanos limestone (4x, crossed Nicol)

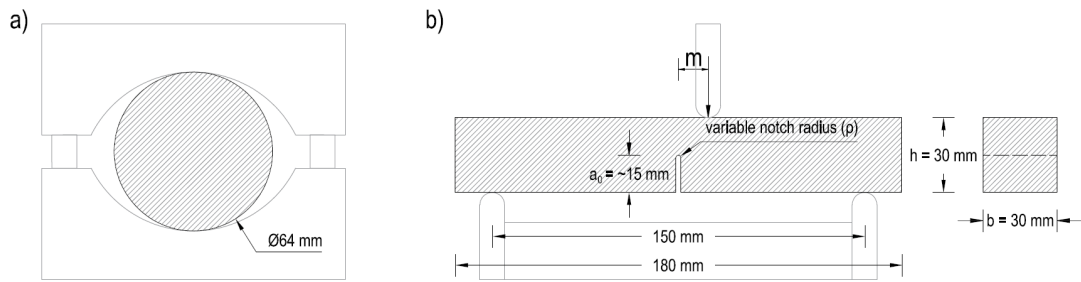


Fig. 2.- Schematic representation of the (a) Brazilian tests and (b) Three-point bending tests.

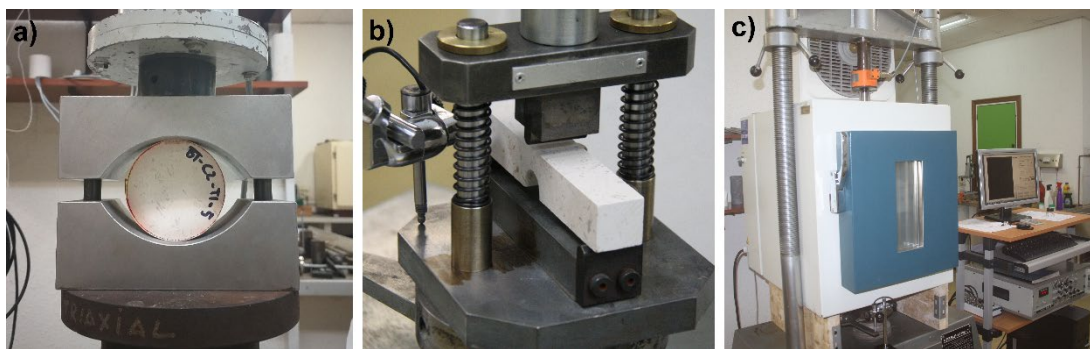


Fig. 3.- Experimental setup of the (a) Brazilian tests, (b) Three-point bending tests and (c) heat chamber coupled to the hydraulic press.

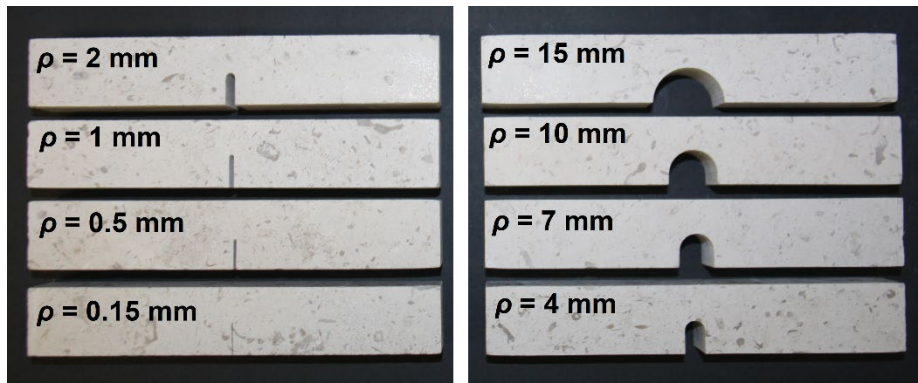


Fig. 4.- Tested SENB samples with different notch radii.

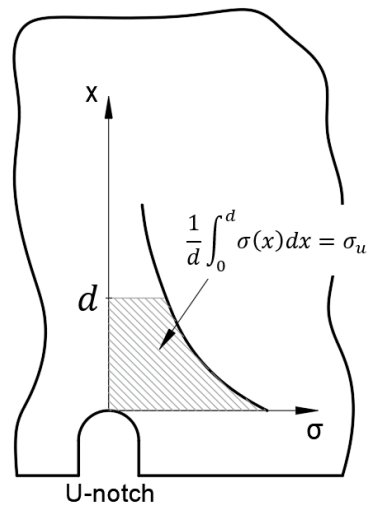


Fig. 5.- Schematic representation of the LM criterion applied on the stress law in the bisector of the notch.

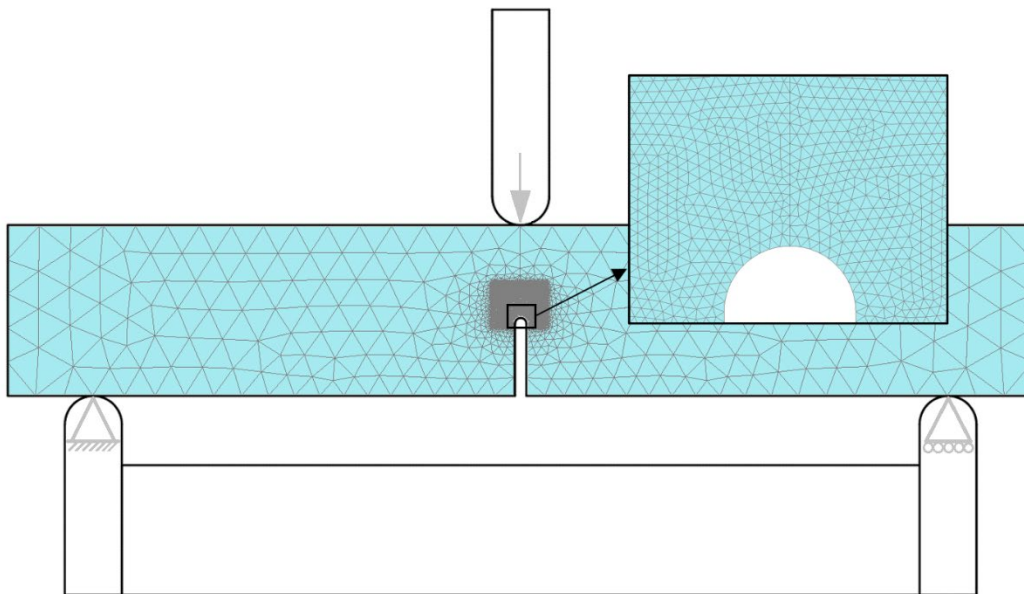


Fig. 6.- Example of a finite element model with the refined region to simulate three-point bending tests (P1, $\rho = 1$ mm).

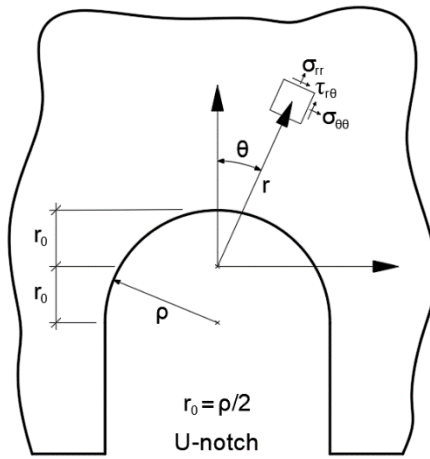


Fig. 7.- Polar coordinate system in U-shaped notches.

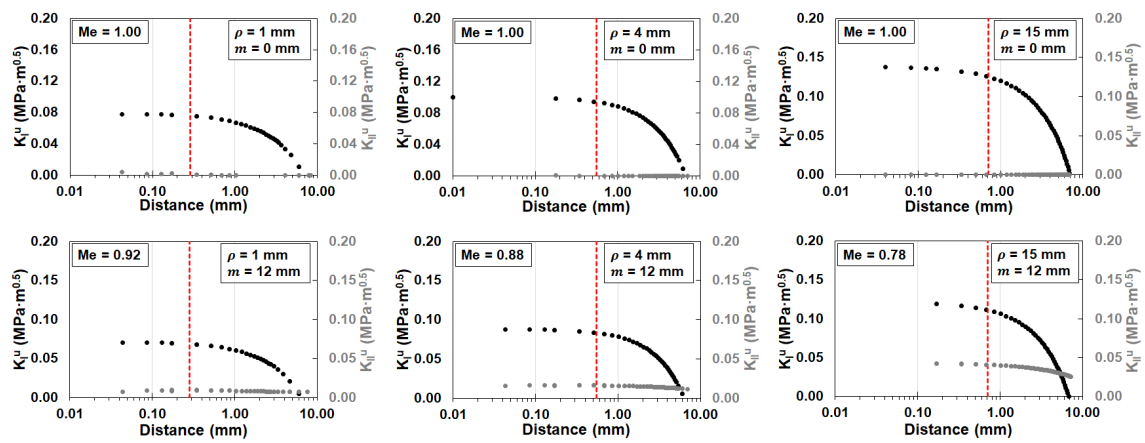


Fig. 8.- NSIFs versus distance for different notch radii ($\rho = 1, 4$ and 15 mm) and loading positions ($m = 0$ and 12 mm) at room temperature.

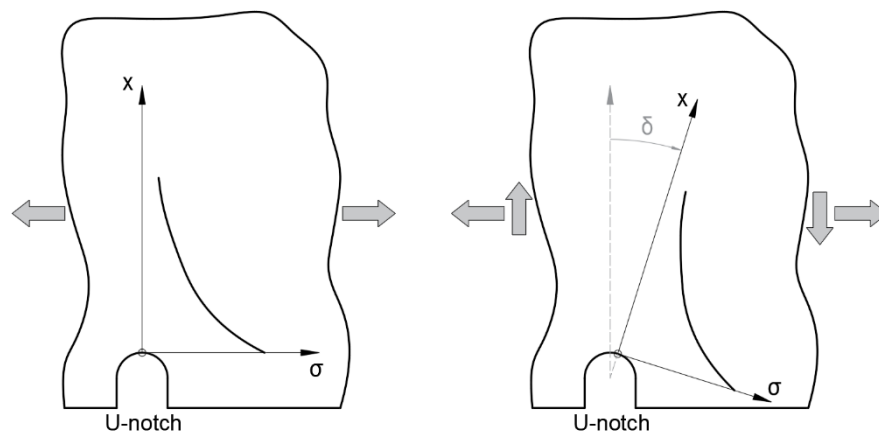


Fig. 9.- Schematic representation of the critical plane and stress-distance curves under (a) mode I and (b) mode I+II loading conditions.

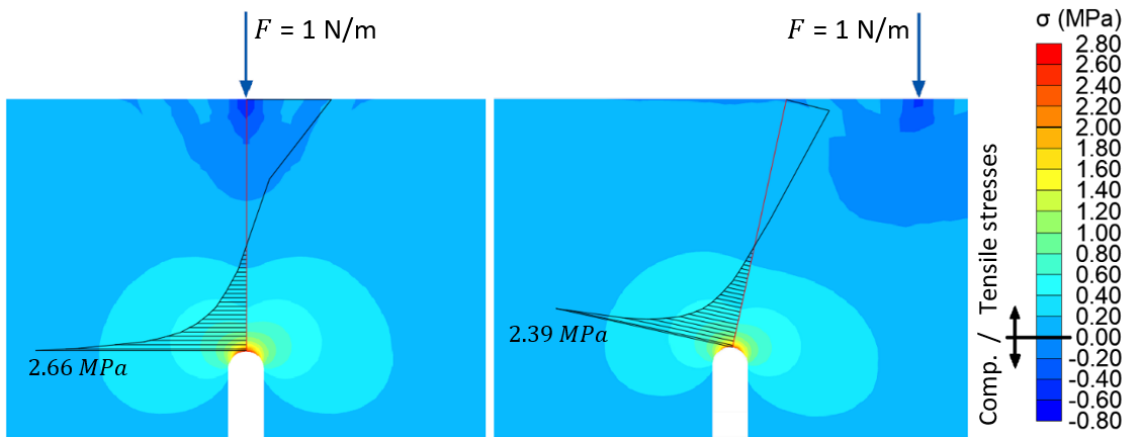


Fig. 10.- Numerically obtained critical planes and stress-distance curves for two different models with $\rho = 1$ mm and (a) $m = 0$ mm and (b) $m = 12$ mm, both of them at room temperature.

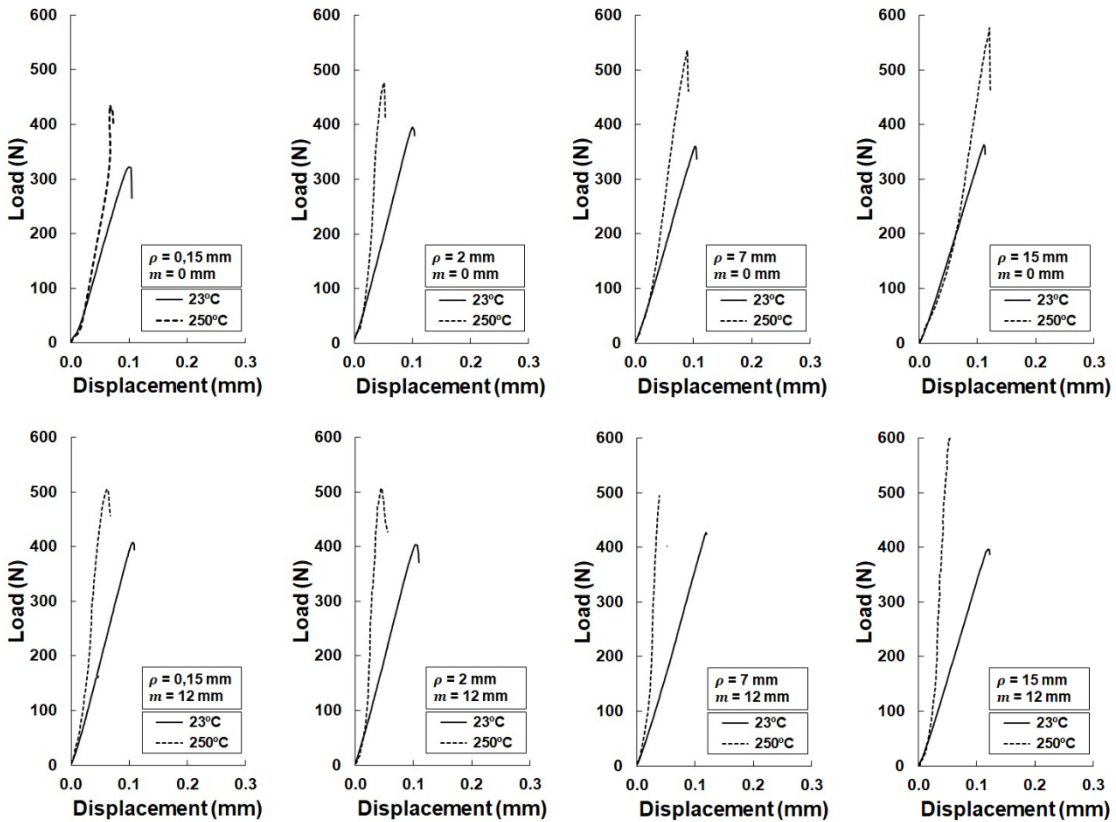


Fig. 11.- Load-displacement curves of the three-point bending tests for different notch radii ($\rho = 0.15, 2, 7$ and 15 mm) and loading positions ($m = 0$ and 12 mm), both for 23°C and 250°C .

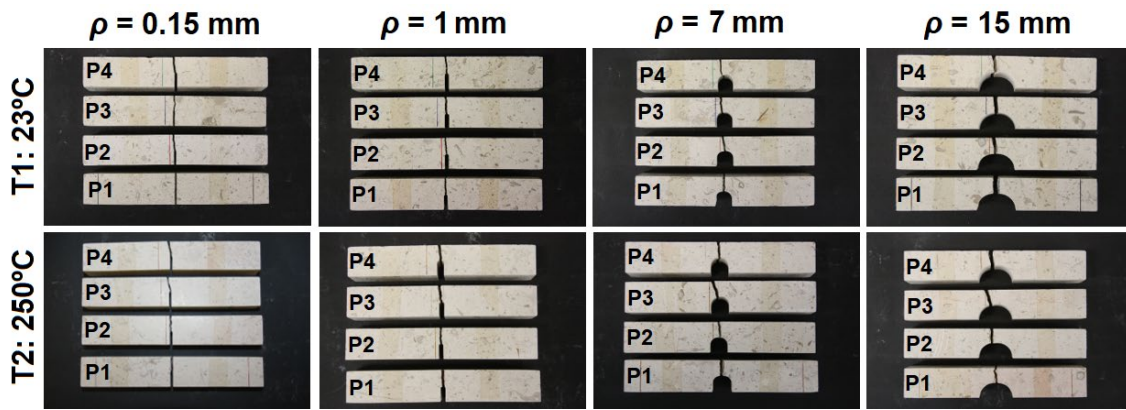


Fig. 12.- Some representative fractured SENB specimens for each loading position and different notch radii ($\rho = 0.15$, 1, 7 and 15 mm), obtained from three-point bending tests at 23°C and 250°C. In all cases the load is applied to the left of the notch.

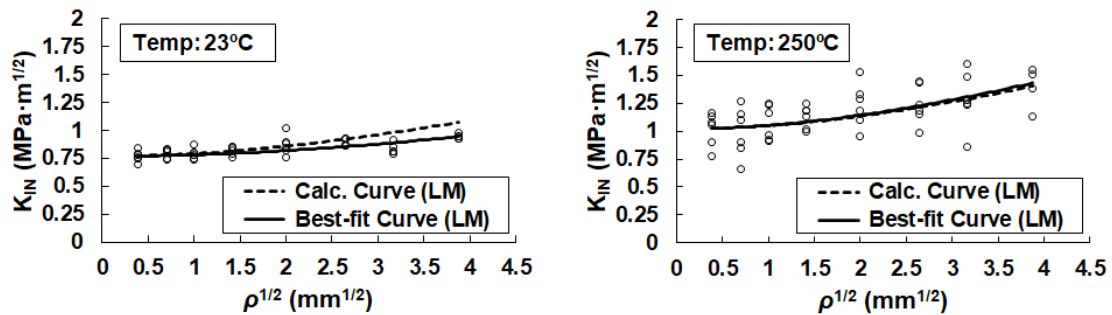


Fig. 13.- Apparent fracture toughness (K_{IN}) versus square root of the notch radius and comparison with the LM of the TCD for both 23°C and 250°C.

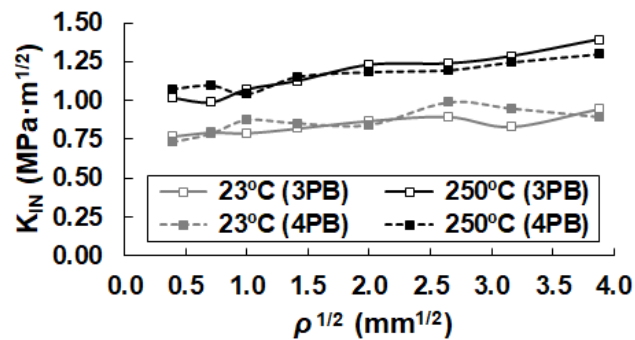


Fig. 14.- Comparison between mean K_{IN} values of the Moleanos limestone obtained from three-point bending and four-point bending (Justo et al. 2020) tests, both at 23°C and at 250°C.

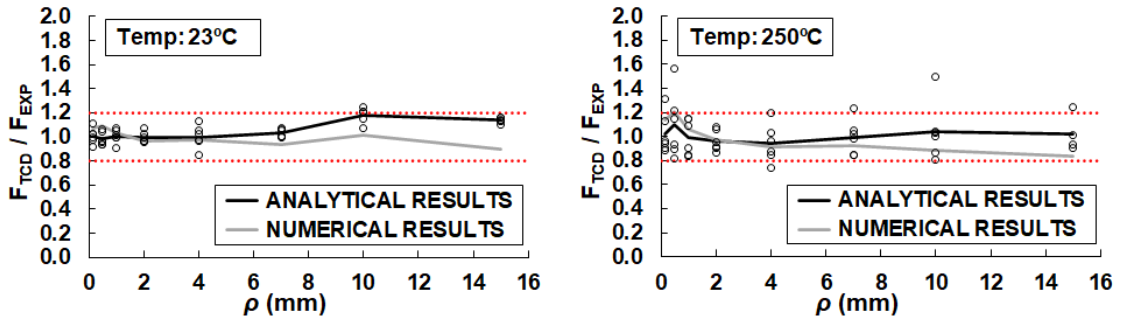


Fig. 15.- Load fracture predictions of the mode I loaded three-point bending tests obtained from the analytical and the numerical analyses according to the LM of the TCD.

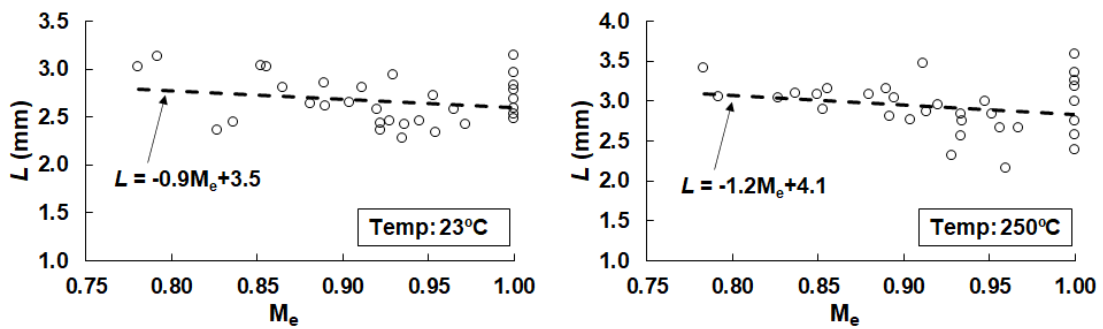


Fig. 16.- Variation of the critical distance (L) with the mode mixity (M_e) at 23°C and 250°C.

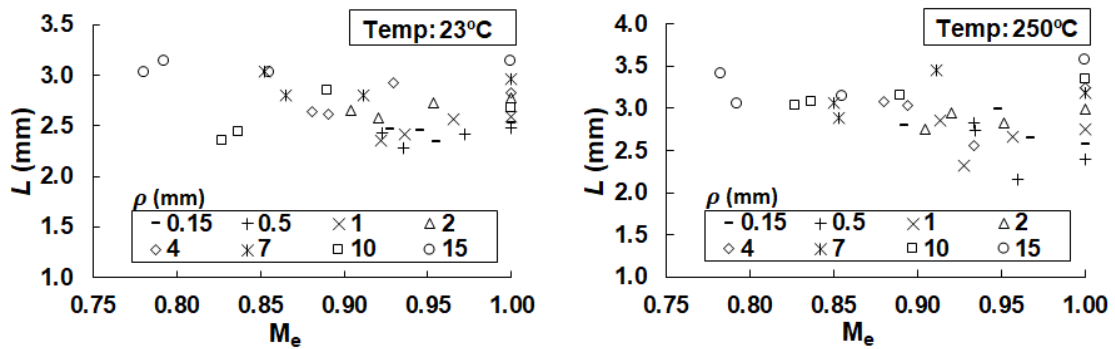


Fig. 17.- Variation of the critical distance (L) with the mode mixity (M_e) at 23°C and 250°C, represented with a different symbol for each notch radius.

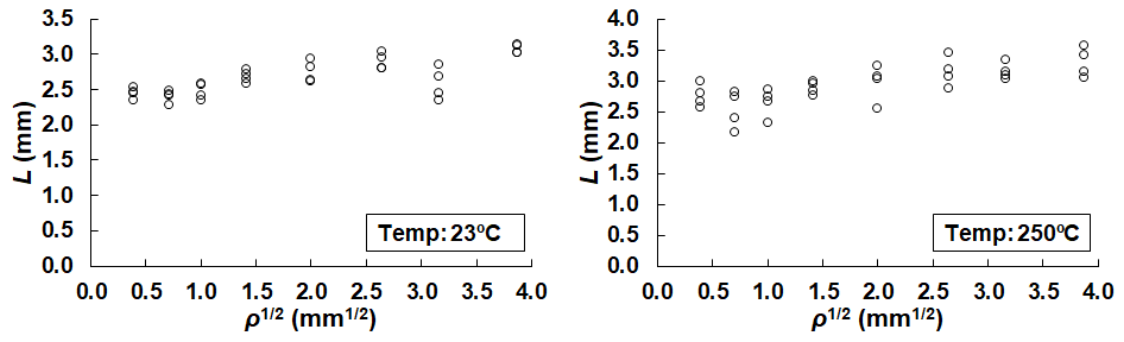


Fig. 18.- Variation of the critical distance (L) with the square root of the notch radius ($\rho^{1/2}$) at 23°C and 250°C.